

Will be submitted to *ISIJ International*

Large Inclusions in Plain-Carbon Steel Ingots Cast by Bottom Teeming

By

Prof. Lifeng Zhang (**correspondence author**)
Department of Materials Science and Engineering
Norwegian University of Science and Technology (NTNU)
Høgskoleringen 8,
7491 Trondheim, Norway.
Tel: 0047-73594123 Fax: 0047-73550203
Email: lifeng.zhang@material.ntnu.no

Mr. Bret Rietow
Formerly master student at Department of Mechanical & Industrial Engineering
University of Illinois at Urbana-Champaign
1206 W. Green St., Urbana,
IL 61801, USA

Prof. Brian G. Thomas
Department of Mechanical & Industrial Engineering
University of Illinois at Urbana-Champaign
1206 W. Green St., Urbana
IL 61801, USA
Tel: 1-217-333-6919 Fax: 1-217-244-6534
Email: bgthomas@uiuc.edu

Ken Eakin
Ellwood Quality Steel Company
700 Moravia St., New Castle, PA 16101
Email: KEAKIN@elwd.com

Abstract

Inclusions in industrial-cast bottom-teemed ingots and runners of plain carbon steel are investigated using ultrasonic detection, optical microscope observation, and SEM analysis. The composition, size distribution, entrapment locations, and sources of ingot inclusions were revealed by examining all the macro-inclusions (larger than 20 μ m) that were observed in 35,000 mm² of sample surface area. Based on 78 non-sulfide inclusions observed, around 3.23×10^7 macro-inclusions per m³ steel exist in the ingot, with a size distribution increasing with decreasing size. Inclusions are distributed uniformly within a given horizontal section through the ingot, but with more found towards the bottom. The largest inclusions exceed 7mm and originated from mold flux in the ingot. The largest inclusion source appears to be reoxidation, as evidenced by 59% of the ingot inclusions composed of pure alumina clusters and lumps. Eroded refractories from the ladle well block and ladle inner nozzle bricks accounted for 31% of the ingot inclusions. Reaction between the high-Mn steel, reoxidation with air, and reaction with silica in the runner bricks caused very large (>7mm) compound inclusions of SiO₂-MnO-Al₂O₃ in the center of runners.

Key words: Steel Ingot, Inclusions, Runner, Mold flux, Alumina, Exogenous Inclusions

1. Introduction and Methodology

Although the fraction of steel produced in the world via ingot casting has decreased to 11.2% in 2003, this still comprised 108.7 million metric tonnes, including about 2.5 million tonnes in US ¹⁾. Ingot casting is still important because some low-alloy steel grades and steel for special applications can only be produced by this process. These include high carbon chromium bearing steel, ²⁾ thick plate, seamless tube, forgings, bars and wire rods.³⁾

The ever-increasing demands for high quality have made the steelmaker increasingly aware of the necessity for products to meet stringent “cleanliness” requirements. Non-metallic inclusions are a significant problem in cast steels that can lead to problems in castings that require expensive casting repairs or rejection. The mechanical properties of steel are controlled to a large degree by the volume fraction, size, distribution, composition and morphology of inclusions and precipitates, which act as stress raisers. For example, ductility is appreciably decreased with increasing amounts of either oxides or sulphides. ⁴⁾ Fracture toughness decreases when inclusions are present, especially in higher-strength lower-ductility alloys. Similar pronounced property degradation caused by inclusions is observed in tests that reflect slow, rapid, or cyclic strain rates, such as creep, impact, and fatigue testing. ⁴⁾ Pomey and Trentini studied the inclusion removal in ingots from with various deoxidants. ⁵⁾ Franklin ⁶⁾, and Miki et al ⁷⁾ obtained a rough inclusion size distribution in steel ingots. Hilty and Kay ⁸⁾, Pickering ⁹⁾, and Lunner ¹⁰⁾ investigated the compound exogenous inclusions in steel ingots by microscope and SEM analysis. Thomas et al ¹¹⁾ and Leach ¹²⁾ investigated the sources of exogenous nonmetallic inclusions in steel ingots. Inclusions, especially large exogenous inclusions are perhaps the most serious problem affecting steel ingots, and arise primarily from the incidental chemical and mechanical interaction of the liquid steel with its surroundings. Refractory erosion of the ladle and metal delivery system introduce inclusions that can impair the quality of what was otherwise very clean refined steel. ^{3, 9, 13-18)} In addition, air entrainment ^{8, 19)} during teeming generates reoxidation inclusions, such as alumina clusters in Al-killed steels, and the turbulent flow and mixing with the teeming flux during the initial entry of steel into the mold can induce flux entrainment ^{20-26) 27)} during solidification. Inclusion distribution in an ingot is affected by fluid flow, heat transfer and solidification of the steel. Two studies ^{10, 28)} of top-poured ingots found larger slag inclusions concentrate in the central bottom portion of the ingot, and in the outer portions of the ingot top. It was reported that increased teeming temperature decreases the amount of inclusions, because it facilitates their floatation removal by natural convection. For a bottom-poured 2t ingot (with taper) of 0.50% C, Al-Si-Killed steel, the high-melting-point inclusions (high alumina) predominate at the bottom of the ingot, while low-melting-point inclusions (sulphide and silicates) are more abundant in its top central portion, due to the mechanism of positive segregation. ²⁹⁾ It should be noticed that most of these papers on inclusions in steel ingots were published before 1990s, and very few are published in recent 15 years.

This current work is part of a larger project to investigate inclusions in bottom-teemed steel ingots by combining computational models and plant experiments conducted at member companies of the Ingot Metallurgy Forum. A survey with responses from six steel ingot producers in the US revealed that the total annual tonnage of bottom-poured ingots where cleanliness is a concern is at least 700,000 tons. Rejections at these companies due to inclusion defects range from 0.2 - 5% with a cost of \$900-3600/tonne (depending on grade). This corresponds to \$10 million per year (assuming a typical rejection rate of 1% at \$1500/ton). From the survey replies, 10-25% of defects sources are estimated to be related to ladle sand/packing sand entrapment, 25-50 from mold flux entrainment, 0-5% from runner erosion, and 0-35% related to other exogenous inclusion sources. In addition to the above exogenous inclusion sources, the companies estimated that 0-15% of their defects were from alumina inclusions (deoxidation products), 0-20% from air absorption, 0-5% from reoxidation reactions with slag and refractory, and 0-10% from unknown sources. Clearly, exogenous defects are the greatest problem. The actual amount and nature of these inclusion sources is investigated in the present work, based on industrial trials conducted at Ellwood Quality Steels Co.

2. Process Description and Methodology

This work investigates large inclusions measured in a bottom-teemed ingot of 1022 carbon steel, with a composition (ladle analysis) shown in Table 1.

The ingot casting process of concern is shown figure 1 and is described as follows:

- Step1: Scrap is loaded into clam-shell buckets and charged into an ultra high powered (UHP) eccentric bottom tapping furnace (EBT) electric arc furnace. The scrap is melted and refined to remove carbon and phosphorus using an oxidizing slag.
- Step2: The EBT feature minimizes heat loss and allows the liquid steel to be tapped relatively slag-free into the ladle for further refining. During tapping, alloy additions are charged, including aluminum for deoxidation, followed by the addition of a reducing top slag.
- Step3: The ladle is transferred to a treatment station for heating, alloy adjustment and further refining. Arc heating and induction stirring at this step ensures mixing and interaction between the steel and the slag.
- Step4: The steel bath undergoes vacuum degassing where the hydrogen level is lowered to less than 1ppm. Induction and argon gas stirring are combined during this step to optimize stirring energy.
- Step5: The ladle is transferred to a second treatment station, where the steel may be reheated, calcium treated via wire feeding. Final alloy adjustments are made as needed.
- Step6: Heats are bottom teemed into ingots at a designated temperature and a controlled rate of rise. Argon shrouding may be employed prior to teeming to minimize reoxidation and the pick-up of hydrogen and nitrogen. Argon shrouding was not used on the test ingots of this study, however.

For ladle opening, a slide gate is used. The free-open percentage is only about 50%. This low percentage is a concern because it is well known from studies of continuous casting that lance-opening of ladles induces serious reoxidation, increasing total oxygen (T.O.) oxygen in the tundish to 10ppm higher than that by free opening.³⁰⁾ The ladle slag was mainly CaO. Visual observation is the only method used to detect and prevent slag carryover into the trumpet during teeming, so the standard practice also requires extra metal in the ladle, so no slag pours into the trumpet. The teeming process delivers the steel down a trumpet, through a “spider” distributing the flow into 7-8 round-section runners with inner diameter of 50.8mm, across and up through inlets with the same diameter into each mold in a cluster of 7-8 ingots. The compositions of the mold flux and refractories are shown in Table 2 and Figure 2, including the ladle lining, well block, filler sand, trumpet, and runner bricks. Some of the refractory contains high SiO₂, which is known to cause severe reoxidation of molten steel.³¹⁾

The ingots in this study were round with 0.33m diameter, 4.70m height and 2.91 metric tonnes in weight. The total filling rate was around 1.4 tonne/min (23kg/s), with 3.3kg/s to each ingot. This increased the ingot level at 4.87mm/s. The typical filling time was 13-18 minutes, Mold powder was added by placing a 5-kg bag on the bottom of each ingot prior to teeming. Some operations suspend the bags of powder above the bottom to lessen powder entrapment during the start of filling??. Important topics of interest include the filling rate (rate of rise), the delivery-system geometry, which may cause turbulence and encourage mold powder entrapment, slag entrapment by vortexing near the ladle nozzle at the end of teeming, argon shrouding, and the erosion of refractories.

After final solidification, the ingot was sectioned. Figure 3 diagrams how the samples were obtained, where “A” indicates the direction away from runner from the trumpet. In total, 54 cube-shaped steel samples of 25.4mm (1inch) per side were examined for inclusions. The total observation area was almost 35,000mm². In addition, the solidified runner bar/spider for this ingot was also examined. After polishing, the samples were first observed under an optical microscope to mark the locations of all inclusions larger than 20µm in diameter. Then, the detailed morphology and composition of each inclusion was analyzed by scanning electron microscope (SEM) using Energy

Dispersive X-Ray Analysis. Almost all of the large non-sulfide inclusions were photographed. In addition, several sample photographs were taken of the much more common indigenous sulfide inclusions, and of the numerous holes (voids) that were larger than 20 μm .

The results of these detailed tests were compared with standard industrial tests of ingot cleanliness. Another ingot from the same cluster was cut into two 84-inch lengths with the hot top and ingate left intact. These pieces were forged into $\phi 7.5$ inch bars, measuring 238 inch in length. After machining away 6mm (0.25in.) of the surface layer, inclusions in the resulting $\phi 7$ inch bars, were detected using standard Ultra Sonic Scanning (USS).

2. Ingot Inclusions Analysis

2.1 Ultra Sonic Detection

In the forged bar samples detected by Submerged Ultra Sonic Scanning, only two inclusions were detected. As shown in Figure 4, one of these macro-size nonmetallic inclusions was uncovered at the top end of the bottom bar while trimming the end. This huge defect exceeded 20mm in length, even after forging. It contained O, Na, Mg, Al, Si, K, Mn, S, and Ca, indicating it to originate from mold flux. The fact that so few exogenous inclusions were found by Ultra Sonic Detection indicates that this method can reveal only large inclusions, exceeding ~ 1 mm in diameter. It is crucial to detect such large and rare inclusions. However, determining the true cleanliness of the steel also requires microscope observation and SEM detection.

2.2 Microscope Observation and SEM Detection

Typical inclusions detected by optical microscope observations and the corresponding SEM image of the same inclusions/holes are compared in Table 3. The SEM reveals the true morphology of the defects more clearly than the microscope observations. Defects S1 and S5 appear to look like inclusions under microscope observation. However, the SEM images clearly reveal that S1 is an inclusion cluster with a hole, and S5 is interdendritic porosity. The SEM images also show that S2 is an inclusion cluster rather than a square-shaped inclusion as it appears under the microscope; S4 is an irregular-shaped hole remaining after the inclusions were polished away, rather than a simple inclusion; and S6 is a bubble-shaped circle rather than an inclusion. These results indicate the short-comings of inclusion detection by ultra-sonic detection or optical microscopy alone, and the power of the combining these two methods with detailed SEM analysis of previously-detected inclusions.

2.3 Inclusion Amount and Size Distribution

The total of 78 non-sulfide inclusions larger than $20\mu\text{m}$ that were detected in the ingot are plotted in Figures 5 & 6 according to their location along each bar-sample. In the 11613 mm^2 total area observed at each of three ingot heights, most (47) of these large inclusions were observed on the section near the ingot bottom (sample 5), 29 on the half-height samples, and no inclusions were found on the ingot upper section. Thus, the most important trend in entrapment location is a decrease in inclusions with height up the ingot. At the ingot bottom, inclusions appear to concentrate in two regions, peaking at 40mm from the center line and at 20mm from the surface. At the ingot half height, inclusions are distributed more randomly, although there may be a slight concentration at the ingot surface. At every height, inclusions are randomly distributed around the ingot perimeter, but there may be a slight trend of more inclusions towards the trumpet side of the ingot near the ingot bottom.

The inclusion size distribution from the two-dimensional microscope observations is shown in figure 7, and was converted into the three-dimensional size distribution in figure 8, using Eq.(1).

$$n_{3D} = \frac{n_{2D}}{d_p} \times 10^{12} \quad (1)$$

where n_{2D} is the number of inclusions per mm^2 of steel surface area, d_p is inclusion diameter in μm under microscope observation, n_{3D} is the number of inclusions per m^3 of steel volume. This equation assumes that each inclusion is roughly cylindrical in shape, with height (into the plane) equal to its observed diameter. There are $\sim 3.23 \times 10^7$ total inclusions larger than $20\mu\text{m}$ per m^3 of steel, including 9.57×10^5 inclusions larger than $200\mu\text{m}$ per m^3 steel. The total mass of inclusions larger than $20\mu\text{m}$ is $62.7\text{ mg}/10\text{kg}$ steel, assuming inclusion and steel densities of $3000\text{kg}/\text{m}^3$ and $7800\text{kg}/\text{m}^3$ respectively. If all of these inclusions were Al_2O_3 , they would correspond to 6.27ppm mass fraction and 3ppm total oxygen in the steel. The total number of inclusions in the ingot is much larger than this, however, considering that most of the inclusions are smaller than $20\mu\text{m}$. and sulfide inclusions are not counted. Note in Figs 7 and 8 that the number of inclusions increases consistently with decreasing size, except for the few largest inclusions, which have random sizes, likely due to the small sample size. Assuming the same $\sim 85\%$ fraction of inclusions smaller than $20\mu\text{m}$ as was measured in continuous cast steel (30ppm)³², the ingot likely contains more than 40ppm total inclusions, or 19ppm total oxygen.

2.4 Inclusion Types (Composition)

2.4.1 Pure alumina Clusters

Typical clusters of pure alumina inclusions are shown as S1 and S2 in Table 3 and in figure 9. Of the 78 total non-sulfide inclusions observed in the ingot, the majority (46) were pure alumina, which were almost all larger than $50\mu\text{m}$. Roughly half (25) of these were alumina clusters, while the others were irregular-shaped lumps of alumina. The clusters range from being partially surrounded by steel, as shown in S7 and S10, to being relatively exposed, as shown in S9. Some clusters even had steel trapped inside them, such as S8. Some alumina clusters were caught together in the liquid steel, as shown in S11. The center of S11 was dislodged during polishing and became dirty inside. The individual particles in the alumina clusters range from $1\text{-}5\mu\text{m}$ in diameter.

Possible sources of alumina clusters include deoxidation products, reoxidation by air absorption, Ostwald-Ripening of dendritic alumina, and sintering together (by collision) of many small alumina inclusions. Their composition was measured to be almost pure alumina, so they could not arise from refractory brick or slag. The clustering of deoxidation products is a possible source, but the strong refining practice should have prevented such large quantities with such high purity. The most likely source, at least of the large clusters, is air reoxidation. No perfect dendritic alumina inclusions were observed, which suggests that significant time has passed since original formation of the dendritic alumina in a high-oxygen environment. Air absorption likely took place between the ladle and the trumpet during teeming, or at the top surface of the molten steel in the ingot during filling. During the teeming process of this trial, there was no protection where the ladle drains into the trumpet, so air absorption is likely very severe at that location.

2.4.2 Pure alumina lump inclusions

21 Lump-shaped inclusions of pure alumina were observed on many samples, such as shown in Table 3 (S3) and figure 10. Some inclusions were sliced near their center, while others were sliced through an edge. Some inclusions lumps appear to be an aggregation of many thick needle-shaped alumina inclusions that collided together, such as shown in S3, S12, and S13. Others are simply alumina lumps, such as S14, S15 and S16. The formation mechanism of these lump inclusions needs further investigation.

2.4.3. Alumina clusters with exogenous inclusions

Several multi-component clusters that contained alumina and other exogenous inclusions were observed, as shown in Figure 11. These inclusions likely have a multi-stage formation mechanism. Their complicated composition suggests that alumina particles combined with mold flux, broken lining refractory, and / or ladle slag. Micrograph S17 shows a $\sim 250\mu\text{m}$ irregular cavity with some inclusions remaining inside, which means that most of the inclusion was polished away. The composition at

location 1 is Al₂O₃ 69.94%, MgO 15.84%, FeO 4.79%, K₂O 7.32%, Na₂O 0.76%, ZrO₂ 1.37%, which suggests that this inclusion was from mold flux. The inclusion at location 2 is a pure alumina cluster, larger than 50µm. When large exogenous inclusions move through the liquid steel, they may grow by nucleating other compounds from the supersaturated molten steel, or by simply colliding with other inclusions. Inclusions S18 and S19 are examples of a large alumina cluster capturing exogenous inclusions from the lining refractory (Al₂O₃ 84.41%, MgO 5.77%, FeO 2.96%, CaO 2.57%). Inclusion S19 is comprised of Al₂O₃ 76.71%, MgO 23.29%, and is a compound inclusion cluster.

2.4.4. Al₂O₃-MgO inclusions

Many (17) large inclusions of Al₂O₃-MgO were found, such as shown in S18, S19 in Fig.11, and S20, S21 in figure 12. Their compositions are similar to ladle well block, and their shape is irregular with 20-30 µm size. These inclusions may have formed by erosion of the ladle well block, or by alumina clusters firstly attaching to the surface of the well block as a clog, later becoming dislodged into the liquid steel, perhaps reacting with well block material, and finally being captured by the solidified shell. .

2.4.5. Exogenous inclusions from ladle inner nozzle

Seven inclusions were found to contain Al₂O₃ 94-98%, ZrO₂ 2-6%, which is very similar to the composition of the ladle inner nozzle. The ladle inner nozzle (Al₂O₃ 94.00%, ZrO₂ 2.50, SiO₂ 1.00%, others 2.50%) is the only lining refractory that contains zirconium oxide. Thus, during the teeming process, it appears that the ladle inner nozzle was eroded and dislodged inclusions into the liquid steel, likely due to excessive fluid velocity, high temperature and / or long time. These inclusions are shown in Figure 13. Inclusions S24 and S25 have been partially pulled out during polishing process.

2.4.6. Inclusions from mold flux

Six inclusions were observed that contained high K₂O or Na₂O composition. These inclusions are likely from entrapped mold flux, (S26), or perhaps from broken runner brick, (S27), as shown in figure 14. Some of these inclusions are very large, exceeding 150-600µm.

2.4.7. Silica based inclusions

Two spherical silica-based inclusions larger than 20µm were observed. An example is shown in figure 15, with composition Al₂O₃ 61.23%, SiO₂ 2.83%, CaO 35.94%. These inclusions may have originated from ladle slag. They are not mold flux because there is no K₂O and Na₂O.

2.4.8. Bubble-shaped inclusions

Several different kinds of bubble-shaped defects were observed in the steel samples, such as shown in Table 1 (S6) and in Table 4. These defects contain a ring of inclusions around the former boundary of the bubble, or in its wake. Their composition varies widely, but always include inclusions of pure sulfides (MnS) and usually also compound Al₂O₃-MgO inclusions. Although the individual inclusions are small, the entire defect is dangerously large, with diameter of 50-300µm. These defects are believed to arise through the following mechanism:

- Step 1: A moving bubble collides with inclusions which attach to most of its surface;
- Step 2: Inclusions form a shell around most of the bubble surface;
- Step 3: The gas bubble escapes (argon or CO) or reacts / absorbs in the steel (air bubbles);
- Step 4: The shell of inclusions is filled in with molten steel;
- Step 5: Sulfides precipitate during solidification.

2.4.9. Cavity and Holes

Many different types of cavities and holes were found in the samples. Some of these simply arose during polishing by dislodging inclusions, such as shown in Table 1 (S1, S4), Fig.9 (S11), Fig.11 (S17), Fig.13 (S24 and S25). Spherical bubble-shaped holes were likely created during solidification by the escape of gas bubbles (N₂ bubble, CO bubble, and possible argon bubble), such as shown in S29 and S30 in Table 6. Irregular-shaped holes were created during the final stages of solidification comprise interdendritic cavities called “micro-porosity”. Examples are shown in S5 in Table 1, S36-42 in Table 5, and in Figure 16.

The cavities from micro-porosity form due to liquid feeding problems into the interdendritic spaces, so were more often observed near the ingot center where the mushy zone is larger and liquid feeding is more difficult. They are often associated with sulfides, which concentrate in the same region due to microsegregation of S and Mn. Fig.16 shows several interesting examples. Sulfides are present along the dendrite boundaries (holes) in S37 and S38. The void cluster in S39 illustrates mild microporosity. Closeups of severe microporosity near the ingot centerline, shown in S40 and S42, show the jagged nature of the interior of voids. The void edges are the surfaces of dendrites, as revealed in S41, complete with classic secondary arms. A closeup of the dendrite surface in S43 shows MnS inclusions on the dendrite edges, which are likely the precipitated remnants of an interdendritic liquid film.

2.4.10. Sulfide inclusions

A great number of pure sulfide (MnS) inclusions were found in the steel samples. A few examples, are shown in S6 in Table 1, S29,30,31,32,35 in Table 4, S37, 38 and 43 in Fig.16, and in figure 17. These inclusions often appear in clusters with a large size (exceeding >100μm) and are generally much greater than the individual inclusions. Sulfides tend to concentrate around the boundaries of former bubbles and near interdendritic cavities (S6 in Table 1, S29, 30, 31, 32, 35 in Table 4, S37, 38, 43 in Table 5).

2.5. Summary of Ingot Inclusion Sources

The compositions of all 78 of the observed non-sulfide inclusions are plotted on the ternary phase diagram in Figure 18. In total, 59% of the large inclusions (>20μm) were pure alumina or alumina/FeO inclusions. These inclusions are believed to arise mainly from air reoxidation. The most likely places for air absorption are the connection between ladle and trumpet during teeming, and the top surface of the molten steel in the ingot during filling. Of the remaining inclusions having complex composition, 22% were from ladle well block refractory, 9% from the ladle inner nozzle, 8% from mold flux, and 2% from slag inclusions (not mold flux), as shown in Table 5. No inclusions from runner or trumpet brick were found. Mold flux inclusions are more important than indicated here, because the two huge inclusions detected by ultra-sonic detection are not included. In addition, a much larger number of pure sulfide inclusions and smaller inclusions of all types were also observed.

3. Runner Analysis

3.1 Runner Lining Observations

The used runner bricks, shown in figure 19, were also investigated. A layer of black slag-like material was observed between the runner steel and the surrounding refractory brick that partly adhered to both surfaces. The shape of the steel in the round runners was flattened across the top, presumably due to the combined effects of solidification shrinkage and gravity. The slag layer built up more in this top region of the runner, where it averages ~3mm thick and was 0.3mm thick at the bottom (figure 20). Evidence of the molten steel breaking through cracks in the runner brick and leaking around the bricks is observed as large attached fins in several places (Fig.19). The black slag layer contains gas porosity. Analysis using SEM detection shows that three layers exist in the used brick near the steel: original brick, intermediate layer and reaction layer (runner slag) (Fig.20). The

composition of three layers is shown in Table 6. From the original brick to the reaction layer, the SiO₂ concentration decreases, while the levels of other oxides, including Al₂O₃ and MnO generally increase.

3.2. Inclusions in Runner Steel Samples

Samples of steel in the runners were taken near the upgate (sample R1), half-way along the runner (sample R2), and near the trumpet (sample R3), as shown in figure 21. The runner steel samples were cut into 4 quadrants and observed under optical microscope for inclusions larger than 20µm, which were further analyzed by SEM.

Large central inclusions: Extremely huge inclusions (near upgate, runner midpoint) and large voids (near trumpet) were observed in the center of many of the runner samples. These inclusions exceeded 7mm in size, such as shown in Fig. 21. The morphology and composition of these big inclusions are shown in figure 22. The matrix of the large inclusions contains ~18%Al₂O₃, ~40%SiO₂, ~40%MnO (surface average). Different spots have slightly different compositions. There are many needle-shaped inclusions of pure Al₂O₃, (light crystalline phase) which are around 5-10µm in diameter, and 10-100µm in length. These pure Al₂O₃ needles likely crystallized inside the large central inclusions while they were still liquid. These inclusions are entrained runner slag.

Slag inclusions remain in a liquid state while the steel solidifies. Thus, they can be pushed by the growing dendrite tips, to coagulate and collect at the last place to freeze near the runner center, where macroporosity (voids) are also common. The closeup views of the inclusion boundaries in Fig. 22 clearly show that slag filled in the interdendritic porosity. This filling was incomplete, as indicated by the interdendritic porosity remaining in Figure 23. This figure clearly reveals the dendritic tip shape around the interior of the void.

Although they were found in many runner samples, inclusions rich in MnO were rarely found in the ingot. This suggests that these inclusions require long times for reactions to occur, such as between the liquid steel and the refractories. Thus, they likely form later during teeming, and are more likely to remain in the runner.

Other inclusions: In addition to the large central inclusion, many smaller inclusions > 20µm were observed throughout the sample section. As in the ingot steel samples, many of these were pure alumina inclusions, which indicates steel reoxidation by air absorption. In addition to alumina clusters, there were also many sulfide inclusions and small compound inclusions with high MnO content. Figure 24 shows one of these high-MnO inclusions. They contain more SiO₂ than the inclusions in Fig.22.

The number of inclusions observed in each quadrant is included in figure 25. The inclusions generally show a random distribution between quadrants of the samples near the runner ends, where the flow conditions are complicated. In the mid-length sample, more inclusions are found in the upper half of the runner. This is likely due to the the stable fully-developed pipe flow conditions allowing the lower-density inclusions to drift upwards and redistribute at this location.³³⁻³⁵

3.2. Source of Runner Slag and associated Inclusions

These results suggest that two different reactions caused the black runner slag, composition gradients in the lining, and the resulting inclusions containing SiO₂, MnO, and Al₂O₃: (1) re-oxidation of the steel and (2) Mn reduction of SiO₂ in the brick. The increase of Al₂O₃ near the runner surface (Table 6) indicates that either prior air exposure caused alumina particles that attached to the wall, or that silica in the lining refractory reacted with dissolved Al according to:



Secondly, Mn dissolved in the liquid steel has concentrated onto the refractory surface and reduced some of the silica in the brick to Si according to the follow reaction:



This well-known reaction occurs after the dissolved Al is locally depleted. It increases as the Mn level in the steel increases.³⁶⁻³⁸⁾ A second source of the high MnO in the runner slag layer is from prior air entrainment and reoxidation of steel. The many pure alumina clusters are found in the ingot steel samples, prove that this did occur. If air absorption was high enough, then the oxygen remaining after reacting with dissolved Al can then react with Mn to form MnO. This MnO may deposit on the lining surface, or contribute to MnO inclusions directly.

The reaction (slag surface) layer is easily eroded and entrained into the steel for two reasons. Firstly, the refractory structure is weakened by the reaction. Secondly, at the temperature of liquid steel, the reaction products may be in a liquid state. Thus, inclusion material may easily become entrained into the flowing molten steel to be captured by the solidifying front as defects in the final product.

The gas porosity in the black runner slag is likely caused by CO bubbles produced from the following reaction between carbon in the steel with SiO₂ in the brick³⁷⁾



The above findings explain how runner slag forms from air absorption and interaction between high-Mn molten steel and runner bricks that contain SiO₂. To avoid the quality problems that likely result from this runner slag, it is recommended that SiO₂ in all of the refractories be avoided, by increasing the Al₂O₃ content up to 60%, or by using ZrO₂-based refractories. A comprehensive refractory-lining specification is essential for the production of high quality forging ingots. Consistent acceptable composition, porosity, bulk density and strength of the bricks should be maintained, in order to control inclusion content of the final product.

5. Summary and Conclusions

- A comprehensive investigation of inclusions in industrial bottom-teemed ingots and runners of plain carbon steel was undertaken using ultrasonic detection, optical microscope observation, and SEM analysis with EDX. The composition, size distribution, entrapment locations, and sources of ingot inclusions were revealed from the inclusions larger than 20µm that were observed.
- The largest inclusions exceeded 20mm and originated from mold flux in the ingot.
- Reaction between the high-Mn steel, reoxidation with air, and reaction with silica in the runner bricks caused very large (>7mm) compound inclusions of SiO₂-MnO-Al₂O₃ in the runner center.
- Extrapolation from the 35000mm² of samples observed to the total volume suggests total 3.23×10⁷ inclusions larger than 20µm per m³ steel in the ingot, with a size distribution increasing in number with decreasing size.
- Inclusions are distributed uniformly with the ingot same high section, but with more found towards the bottom.
- The largest inclusion source appears to be reoxidation, as evidenced by 59% of the ingot inclusions composed of pure alumina clusters and lumps.
- Eroded refractories from the ladle well block and ladle inner nozzle bricks accounted for 31% of the ingot inclusions.
- Ingot quality can be improved only by careful control of teeming to prevent air reoxidation, and by maintaining high control of the lining refractories. Silica-containing bricks should be avoided.

- Evaluation of ingot macro-inclusions requires a combination of detection methods, including ultrasonic detection to find the large rare inclusions, optical microscope observation to find the inclusions > 20 microns, and SEM evaluation to confirm the composition and origin of previously-detected inclusions.

Acknowledgements:

This work was supported by a grant from the Ingot Metallurgy Forum, which is gratefully acknowledged. Thanks are also extended to Elwood Quality Castings for conducting the industrial trials, and to Danielle Q. Baird at Timken, Inc. for help with planning. Microscopy was performed using the facilities at the Center for Microanalysis of Materials at the University of Illinois, which is partially supported by the U.S. Department of Energy under grant DEFG02-91-ER45439. Finally, thanks are owed to Jim Mabon and to the Machine Shop at the Department of Mechanical & Industrial Engineering for help with sample preparation.

References:

- 1) *Steel Statistical Yearbook 2002*, International Iron and Steel Institute, Brussels, (2002).
- 2) E. Fuchs and P. Jonsson: *High Temperature Materials and Processes*, (2000), **19**(5), 333.
- 3) K. Sumitomo, M. Hashio, T. Kishida and A. Kawami: *Iron and Steel Engineer*, (1985), (3), 54.
- 4) P. K. Trojan: *ASM International, ASM Handbook*, (1988), **15 (Casting)**, 88.
- 5) G. Pomey and B. Trentini, in International Conference on Production and Application of Clean Steels, eds., The Iron and Steel Institute, London, Balatonfured, Hungary, (1970), 1-14.
- 6) A. G. Franklin, in International Conference on Production and Application of Clean Steels, eds., The Iron and Steel Institute, London, Balatonfured, Hungary, (1970), 241-247.
- 7) Y. Miki, H. Kitaoka, T. Sakuraya and T. Fujii: *Tetsu-to-Hagane*, (1992), **78**(3), 431.
- 8) D. C. Hilty and D. A. R. Kay: *Electric Furnace Steelmaking Conference Proceedings*, (1985), **43**, 237.
- 9) F. B. Pickering, in International Conference on Production and Application of Clean Steels, eds., The Iron and Steel Institute, London, Balatonfured, Hungary, (1970), 75-91.
- 10) S. E. Lunner, in International Conference on Production and Application of Clean Steels, eds., The Iron and Steel Institute, London, Balatonfured, Hungary, (1970), 124-136.
- 11) J. D. Thomas, R. O. Russell and T. R. Garcia, in 69th Steelmaking Conference Proceedings, eds., ISS, Warrendale, PA, (1986), 300-308.
- 12) J. C. C. Leach, in International Conference on Production and Application of Clean Steels, eds., The Iron and Steel Institute, London, Balatonfured, Hungary, (1970), 105-114.
- 13) M. M. McDonald and D. C. Ludwigson: *the American Society for Tesing and Materials, Journal of Tesing and Evaluation*, (1983), **11**(3), 165.
- 14) Special Report No.63: Ingot Surface Defects Sub-Committee (Steelmaking Division) of the British Iron and Steel Research Association, Report No., (1958).
- 15) P. W. Wright: *Metals Forum*, (1979), **2**(2), 82.
- 16) S. Riaz, K. C. Mills and K. Bain: *Ironmaking and Steelmaking*, (2002), **29**(2), 107.
- 17) G. B. Hassall, KG; Jones, N; Warman, M: (2002), **29**(5), 383.
- 18) R. L. Shultz: *Steelmaking Conference Proceedings*, (1979), **62**, 232.
- 19) R. Schlatter: *Steel Times*, (1986), (8), 432.
- 20) A. Staronka and W. Golas: *Arch. Eisenhüttenwes.*, (1980), **51**(10), 403.
- 21) P. Kazakevitch and M. Olette, in International Conference on Production and Application of Clean Steels, eds., The Iron and Steel Institute, London, Balatonfured, Hungary, (1970), 42-49.
- 22) A. W. Cramb and I. Jimbo: *Iron & Steelmaker (ISS Trans.)*, (1990), **11**, 67.
- 23) K. Suzuki, K. Taniguchi and T. Takenouchi: *Tetsu-to-Hagane*, (1975), **61**(4), S96.
- 24) I. Manabu, S. Yutaka, O. Ryusuke and M. Zen-Ichiro: *Tetsu-to-Hagane*, (1993), **79**(5), 33.
- 25) H. F. Marston, in 69th Steelmaking Conference Proceedings, eds., ISS, Warrendale, PA, (1986), 107-119.
- 26) J. G. Bartholomew, R. L. Harvey and D. J. Hurtuk, in 69th Steelmaking Conference Proceedings, eds., ISS, Warrendale, PA, (1986), 121-127.
- 27) A. P. Ogurtsov: *Steel in the USSR*, (1988), **18**, 225.
- 28) Z. Chen, J. Liu and J. Zeng: *Iron & Steel (China)*, (1983), **18**(3), 43.
- 29) M. D. Maheshwari and T. Mukherjee: *Tisco*, (1979), **26**(1), 9.
- 30) K. P. Hughes, C. T. Schade and M. A. Shepherd: *Iron & Steel Maker*, (1995), **22**(6), 35.
- 31) L. Zhang and B. G. Thomas: *ISIJ Internationla*, (2003), **43**(3), 271.
- 32) L. Zhang, B. G. Thomas, K. Cai, L. Zhu and J. Cui, in ISSTech2003, eds., ISS, Warrandale, PA, (2003), 141-156.
- 33) L. Zhang and B. G. Thomas: Continuous Casting Consortium, University of Illinois at Urbana-Champaign, Report No., (2005).

- 34) L. Zhang and B. G. Thomas: Continuous Casting Consortium, University of Illinois at Urbana-Champaign, Report No., (2005).
- 35) L. Zhang and B. G. Thomas: Continuous Casting Consortium, University of Illinois at Urbana-Champaign, Report No., (2005).
- 36) S. M. Kim, L. W-K, P. S. Nicholson and A. E. Hamielec: *American Ceramic Society Bulletin*, (1974), **53**(7), 543.
- 37) N. Reitsema and P. W. Wright: *1st International Conference on Refractories*, (1983), 795-810.
- 38) A. Muan: *Electric Furnace Steelmaking Conference Proceedings*, ISS, USA, (1985), **43**, 384-388.

Captions:

Table 1	Steel composition in the trial
Table 2	Composition of flux and linings used at ladle, trumpet, runner and ingot mold
Table 3	Comparison of 2D microscope and 3D SEM images of typical inclusion-related defects
Table 4	Bubble-shaped inclusion defects
Table 5	Sources of >20 μ m inclusions in ingot
Table 6	Composition of the used runner brick and runner slag
Fig.1.	Schematic of ingot production process
Fig.2	Schematic of bottom teeming process
Fig.3	Schematic of sampling locations in 13inch round ingot (A is away from the trumpet)
Fig.4	Large nonmetallic inclusions found in the forged ingot
Fig.5	Inclusions (>20 μ m) observed at 280mm from bottom (left) and half height (2350mm from the bottom) (right) of the ingot
Fig.6	Inclusions (>20 μ m) in ingot samples (A: direct away from trumpet, B & C: close to the trumpet)
Fig.7	Two-dimensional size distribution of inclusions by microscope observation
Fig.8	Three-dimensional inclusion size distribution
Fig.9	Morphology of pure alumina clusters
Fig.10	Morphology of lump pure alumina inclusions
Fig.11	Alumina clusters with exogenous inclusions
Fig.12	Al ₂ O ₃ -MgO inclusions
Fig.13	Exogenous inclusions from ladle inner nozzle
Fig.14	Inclusions from mold flux and runner brick
Fig.15	Silica based inclusions
Fig.16	Cavity and holes found on the steel samples
Fig.17	Sulfide inclusions
Fig.18	Composition of non-sulfide inclusions observed in the samples
Fig.19	Used Runner Brick
Fig.20	Runner slag
Fig.21	Runner steel samples (near upgate, runner midpoint, and near trumpet from left to right)
Fig.22	MnO-rich inclusions at the center of runner steel samples
Fig.23	MnO-rich inclusions distribute along the dendritic gap
Fig.24	MnO-rich inclusions near the edge of runner steel samples
Fig.25	Inclusion distribution on runner steel samples

Table 1 Steel composition in the trial

Elements	[C]	[P]	[S]	[Al]	[Si]	[Mn]	[Ni]	[Cr]	[Mo]	[Cu]
%	.22	.011	.014	.029	.26	1.01	.09	.11	.02	.17

Table 2 Composition of flux and linings used at ladle, trumpet, runner and ingot mold

	Ladle Lining						Nozzle Sand	Trumpet & Runner		Mold Flux
	Wall	Bottom	Well block	Inner Nozzle	Slide gates	Collector Nozzle		Brick	Filler	
SiO ₂	0-5	0.8	0.10	1.00	0.5	10-13	27.6	50.8	0.9	29.0-36.0
Al ₂ O ₃	0-5	0.5	91.22	94.00		83-87	11.8	44.5	0.8	15.0-21.0
MgO	80-100	40.1	6.01	Trace	97.0		7.1	0.1	37.7	<2.0
CaO		57.6	2.51	Trace	1.8		0	0.1	55.6	1.0-5.0
Fe ₂ O ₃	0.5	0.9	0.03		0.2	1-2	18.6	1.0	4.2	5.0-11.0
Na ₂ O			<0.02	0.20		<1		0.47		4.0-6.0
K ₂ O										<2.0
TiO ₂			0.02			1-3		2.1		<1.5
ZrO ₂				2.50			0			
Cr ₂ O ₃							32.9			
MnO										<1.0
F										<0.5
C _{total}	5-15						0.6			23.0-26.0

Table 3. Comparison of 2D microscope and 3D SEM images of typical inclusion-related defects

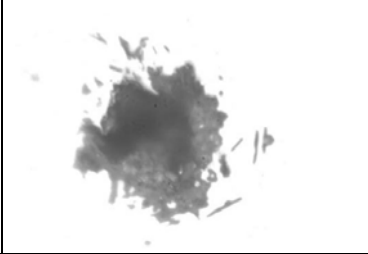
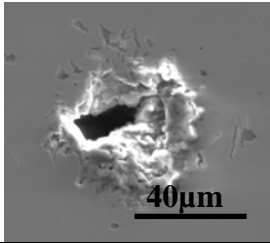
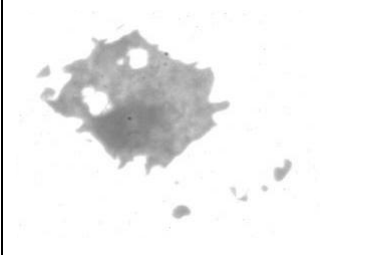
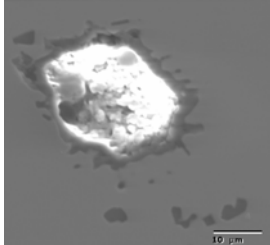

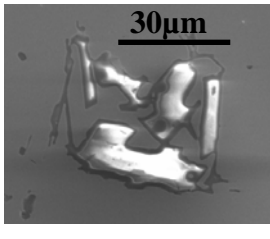
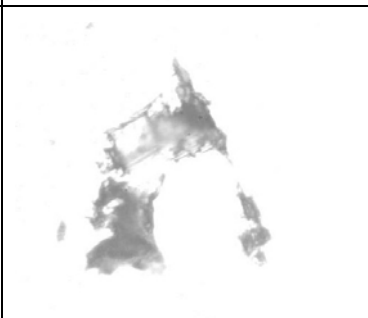
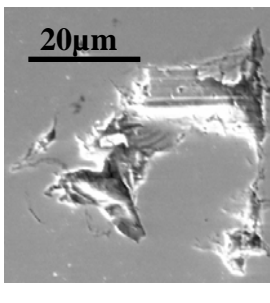
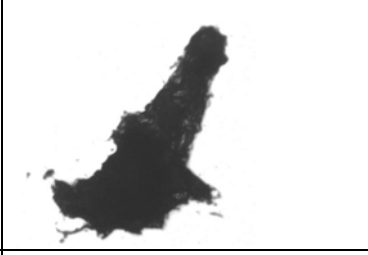
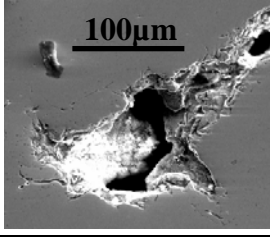
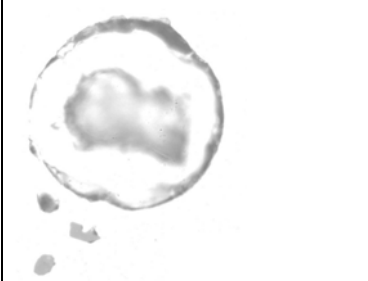
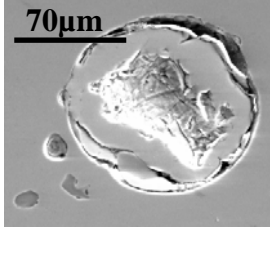
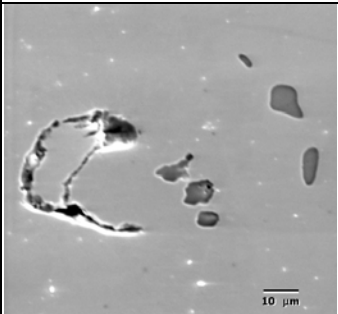
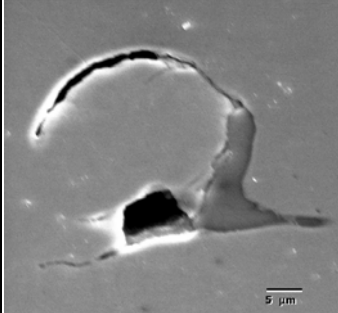
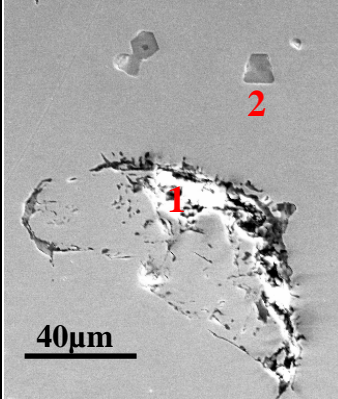
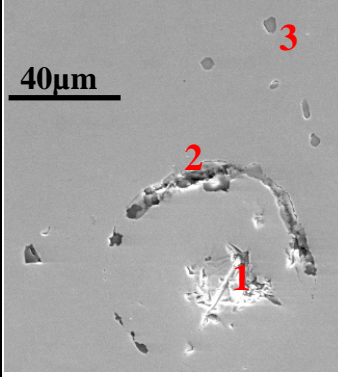
	Two dimensional microscope observation	Three-dimensional SEM detection	
S1			Partially-dislodged pure alumina cluster
S2			Pure alumina cluster
S3			Pure alumina lumps
S4			Irregular-shaped hole remaining after inclusion was polished away
S5			Hole between dendrite arms caused by micro-porosity
S6			Bubble-shaped cavity with sulfide inclusions in its wake.

Table 4 Bubble-shaped inclusion defects

	SEM detection		Composition (%)	Description / Source
S29			MnS	Sulfide (likely precipitated onto former bubble surface during solidification)
S30			MnS	Sulfide (likely precipitated onto former bubble surface during solidification)
S31		1	Al ₂ O ₃ 90.76 FeO 9.24	Alumina aluster (from reoxidation) and sulfide inclusions around the surface of a bubble-like cap (air)
		2	MnS 100	
S32		1	SiO ₂ 21.84 MnO 1.00 FeO 77.16	Mold flux, reoxidation Inclusions around the boundary of a bubble-cap (Sulfide)
		2	MgO 15.52 SiO ₂ 0.60 MnS 15.42 CaO 1.51 MnO 18.75 FeO 48.20	
		3	MnS 100	

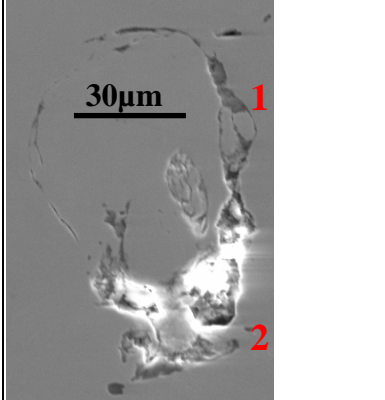
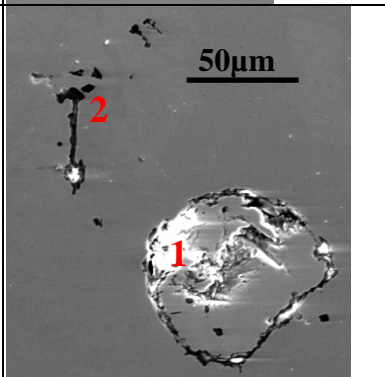
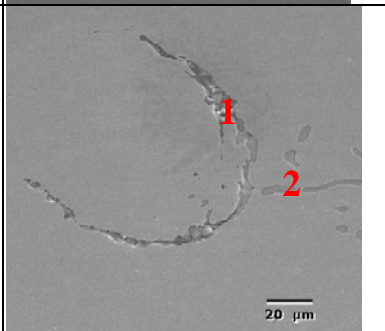
S33		1	Al_2O_3 78.17 MgO 11.61 FeO 10.22	Inclusion cluster (alumina from reoxidation plus ladle lining) at the boundary of a former air bubble
		2	Al_2O_3 76.23 MgO 15.61 FeO 8.16	
S34		1	Al_2O_3 83.32 MgO 16.68	Inclusion cluster (alumina from reoxidation plus runner, trumpet or ladle bottom lining) attached to the boundary of a former air bubble
		2	Al_2O_3 83.88 MgO 5.97 CaO 7.29 FeO 2.85	
S35		1	Al_2O_3 84.05 MgO 15.95	Compound inclusion (alumina from reoxidation and ladle lining) along boundary of a former air bubble Sulfide
		2	MnS	

Table 5 Sources of >20 μ m inclusions in ingot

	Number	Percentage (%)
Alumina (air reoxidation)	46	59%
ladle well block	17	22%
Ladle inner nozzle	7	9%
Mold flux	6	8%
slag inclusions (not mold flux)	2	2%
trumpet and runner bricks	0	0%

Table 6 Composition of the used runner brick and runner slag

	Original brick		Intermediate layer	Reaction layer (runner slag)
	Analysis 1	Analysis 2		
SiO ₂	59.15	52.49	27.11	17.99
Al ₂ O ₃	34.79	45.04	68.63	52.56
MnO	0.01	0.00	1.15	20.01
Na ₂ O	0.14	0.66	1.46	1.73
K ₂ O	1.69	1.30	1.20	1.22
TiO ₂	2.25	0.20	0.25	1.72
Fe ₂ O ₃	1.97	0.31	0.20	4.77

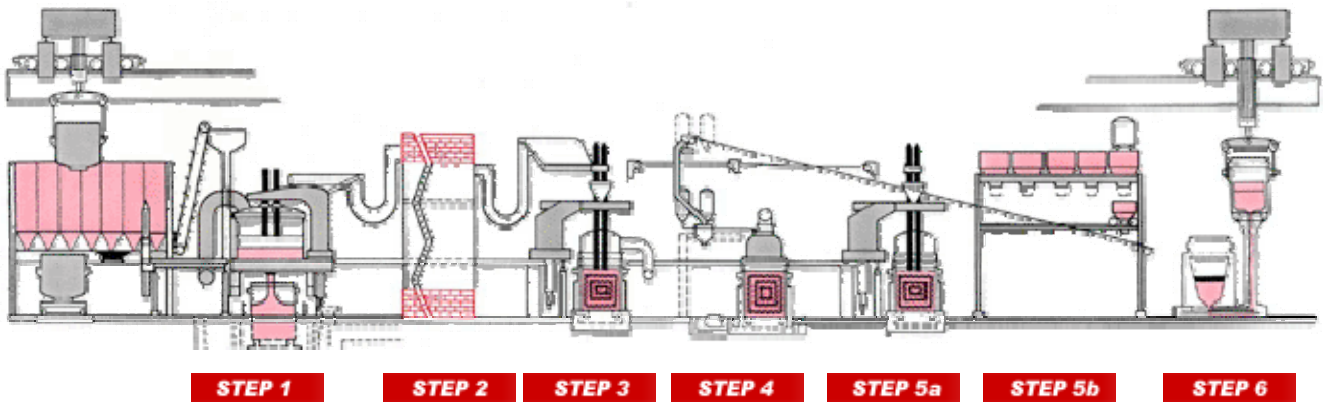


Fig.1. Schematic of ingot production process

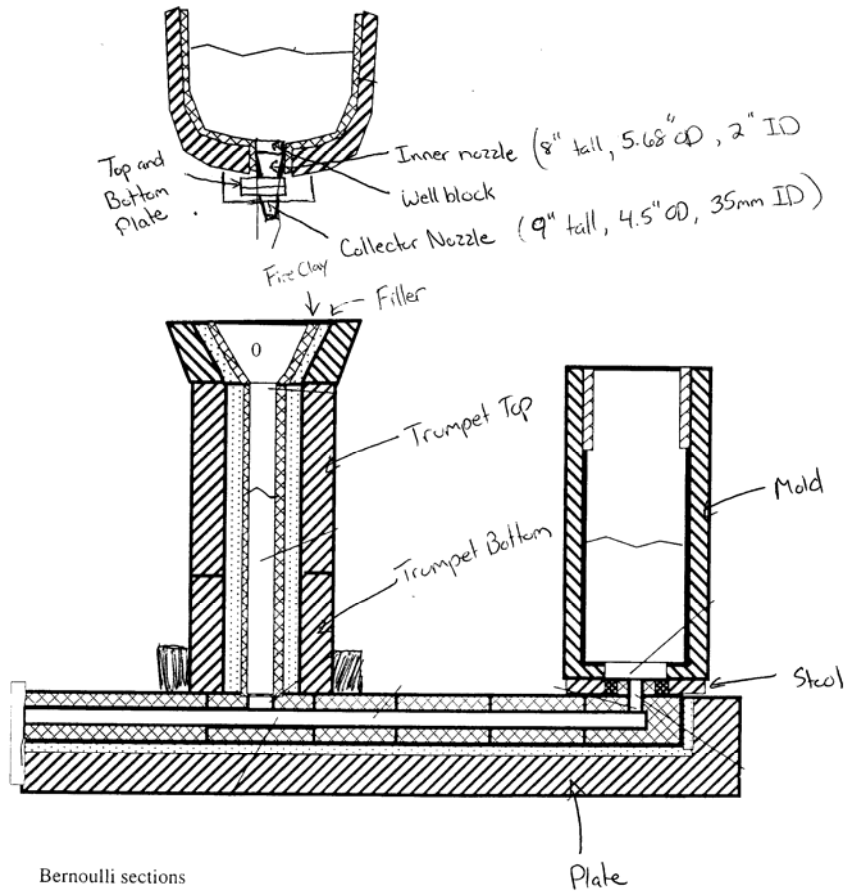


Fig.2 Schematic of bottom teeming process

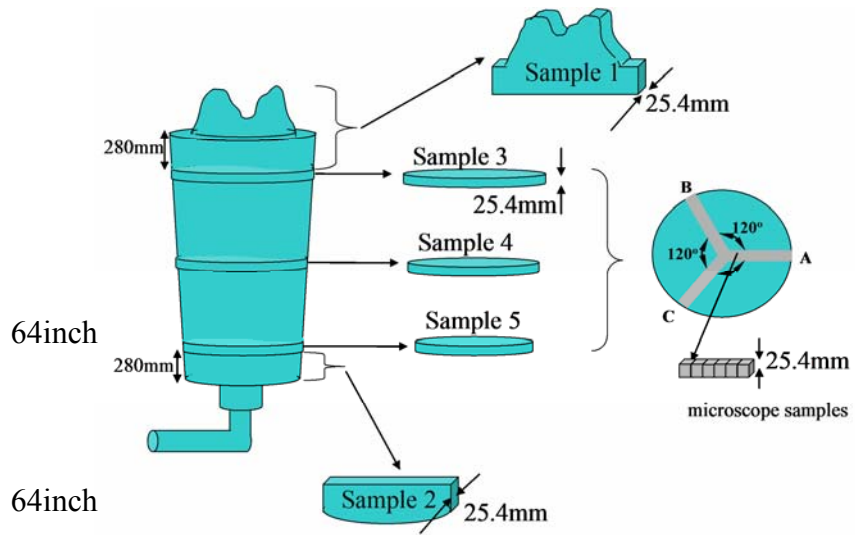


Fig.3 Schematic of sampling locations in 13inch round ingot (A is away from the trumpet)

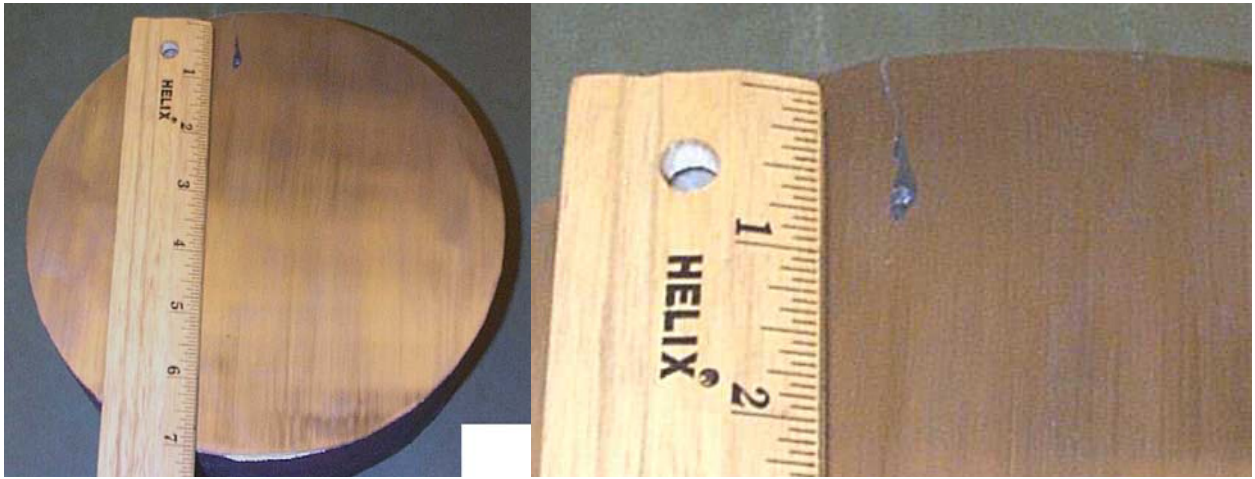


Fig.4 Large nonmetallic inclusions found in the forged ingot

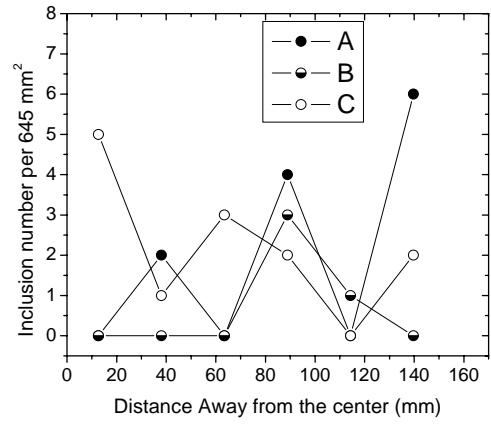
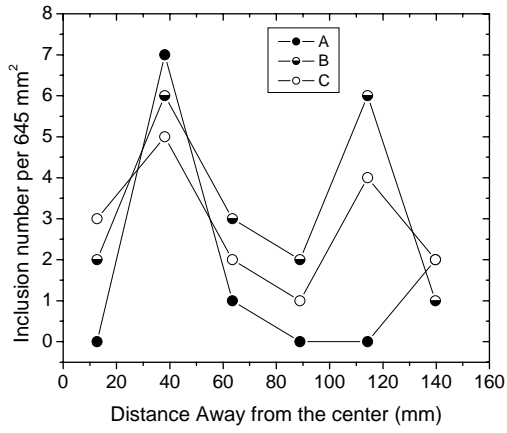


Fig.5 Inclusions (>20 μ m) observed at 280mm from bottom (left) and half height (2350mm from the bottom) (right) of the ingot

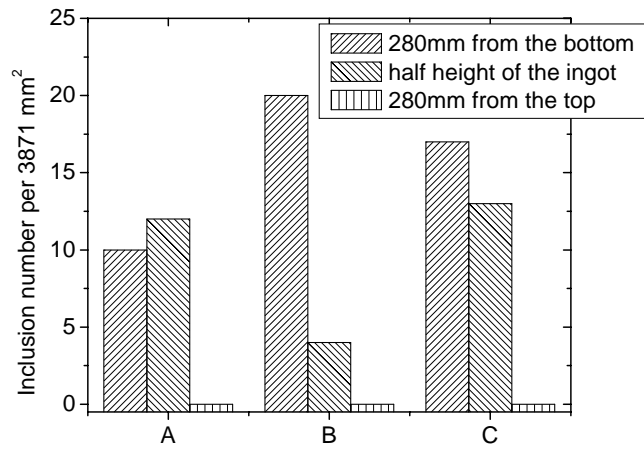


Fig.6 Inclusions (>20 μ m) in ingot samples (A: direct away from trumpet, B & C: close to the trumpet)

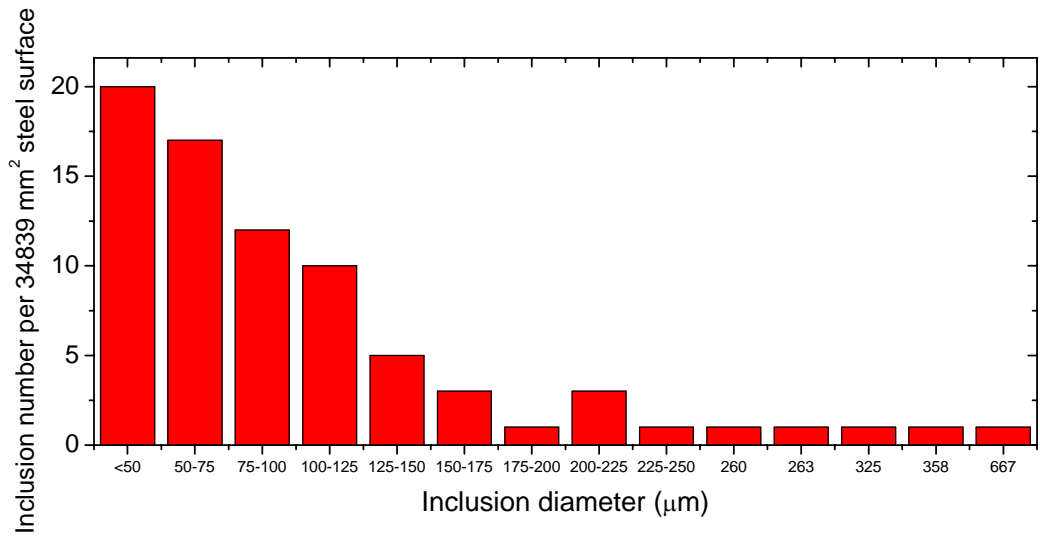


Fig.7 Two-dimensional size distribution of inclusions by microscope observation

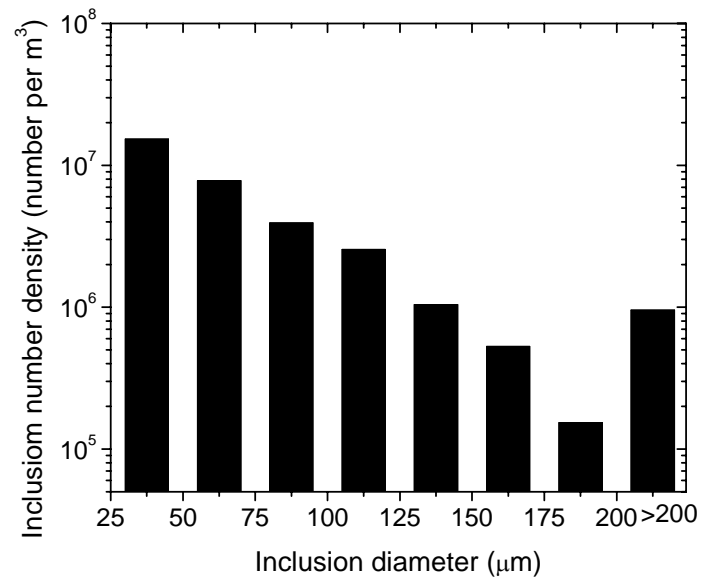
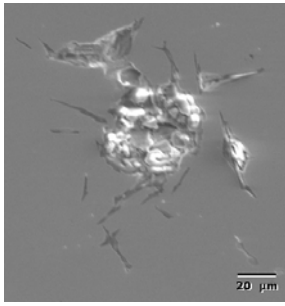
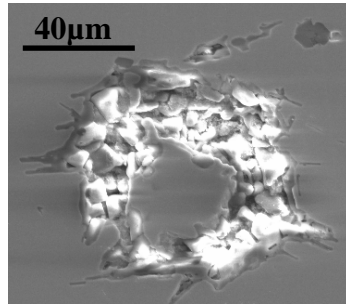


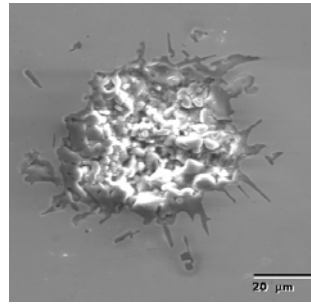
Fig.8 Three-dimensional inclusion size distribution



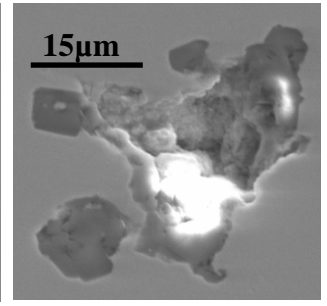
S7



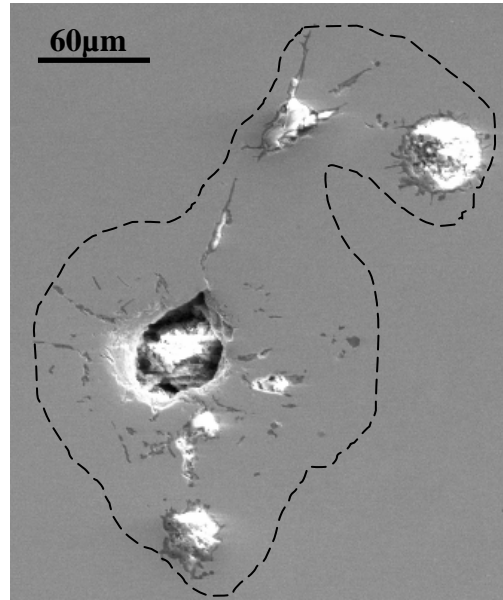
S8



S9

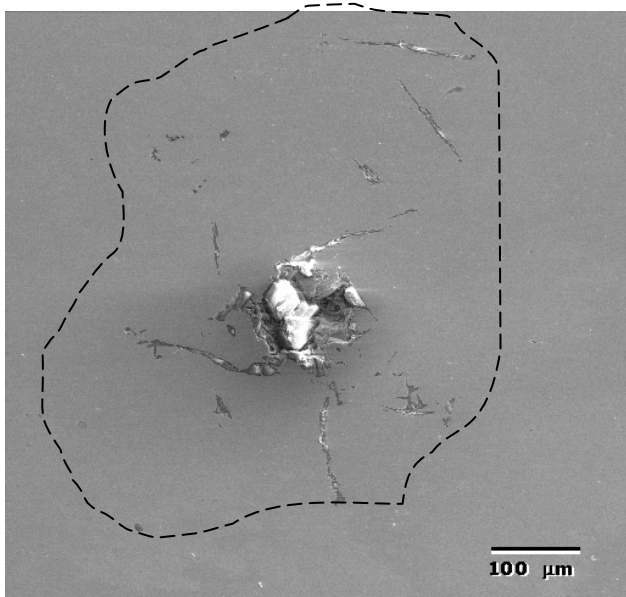


S10

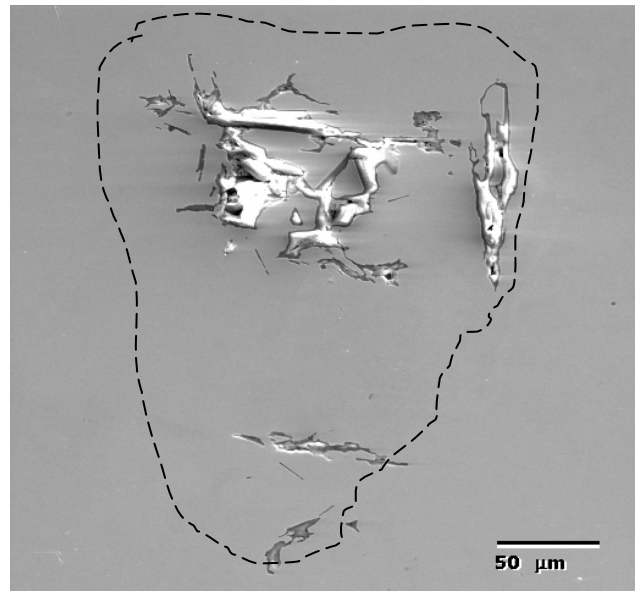


S11

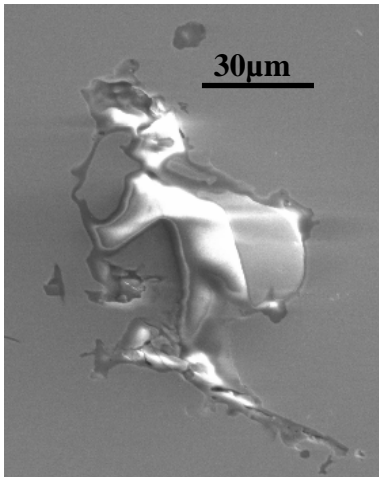
Fig.9 Morphology of pure alumina clusters



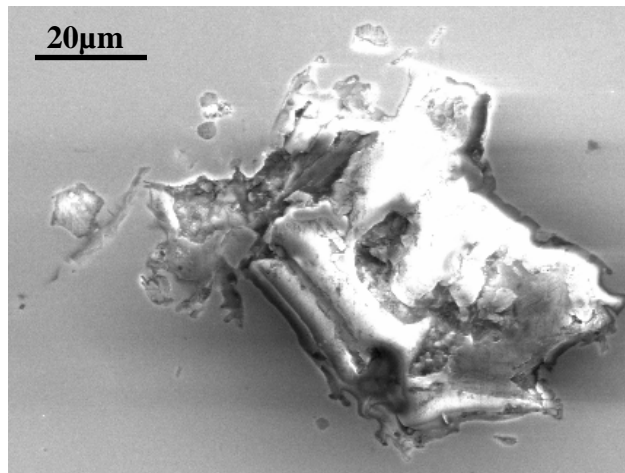
S12



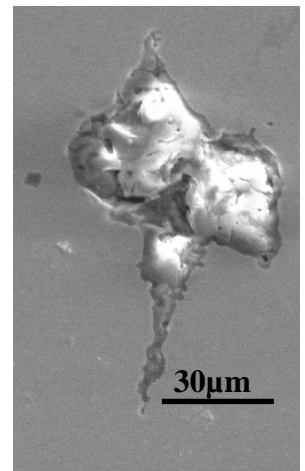
S13



S14

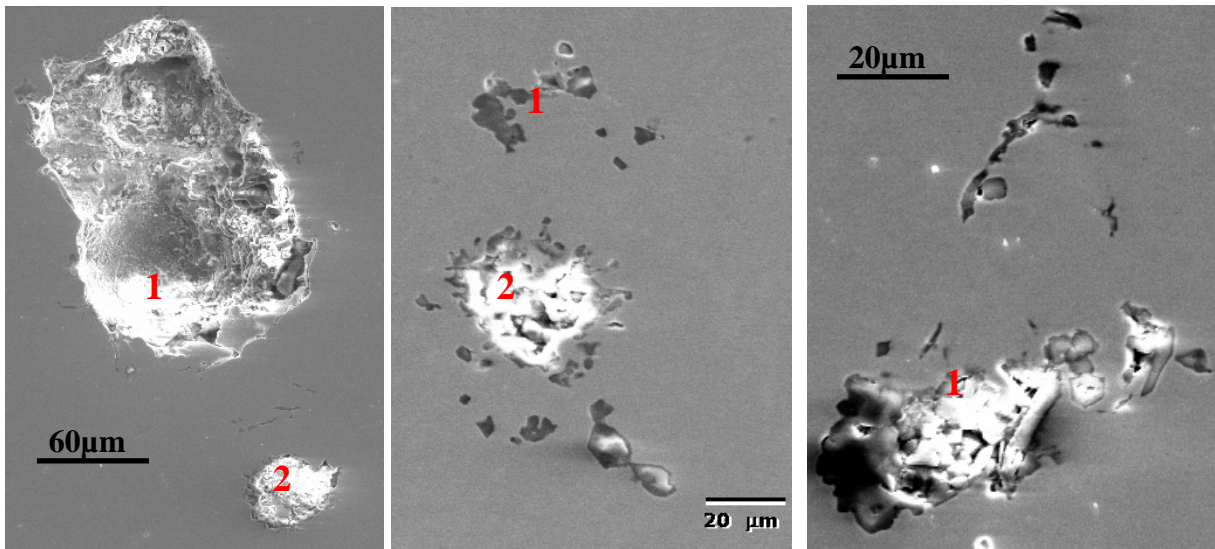


S15



S16

Fig.10 Morphology of lump pure alumina inclusions

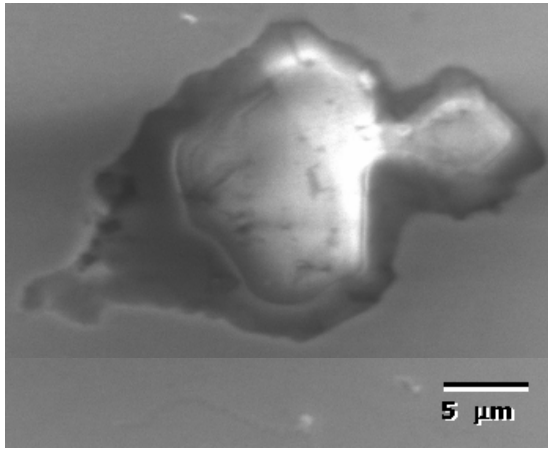


S17

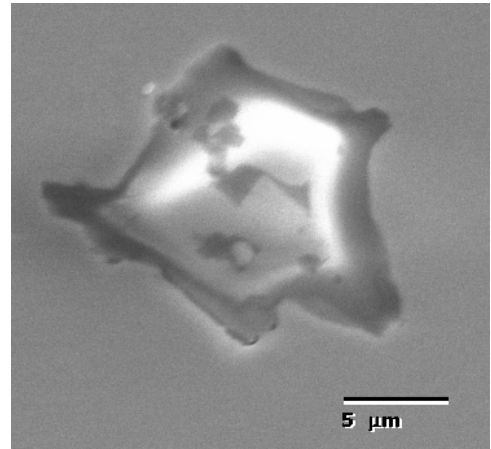
S18

S19

Fig.11 Alumina clusters with exogenous inclusions

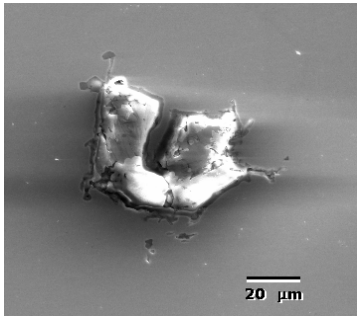


S20 (Al_2O_3 71.72, MgO 23.56, FeO 1.82, MnO 2.90)

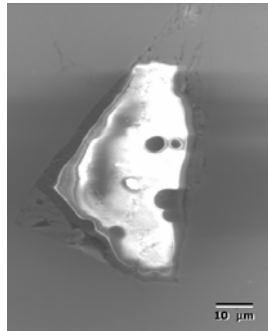


S21 (Al_2O_3 89.26, MgO 10.74)

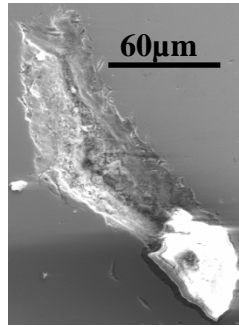
Fig.12 Al_2O_3 -MgO inclusions



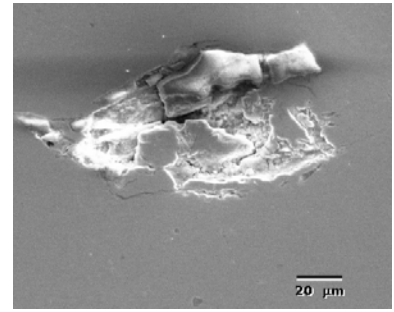
S22



S23

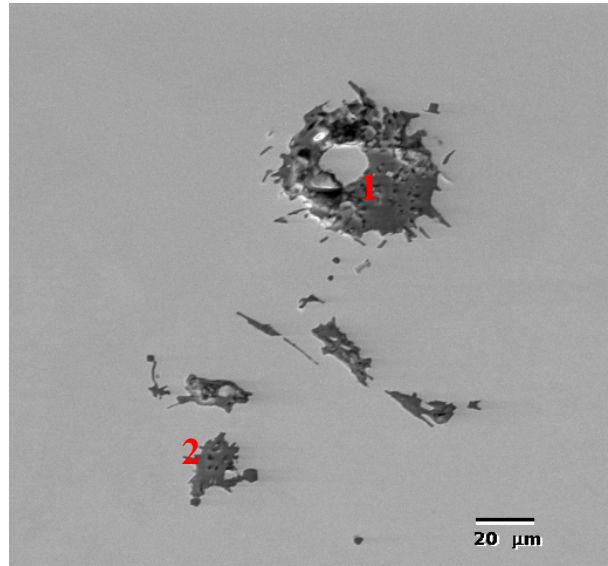
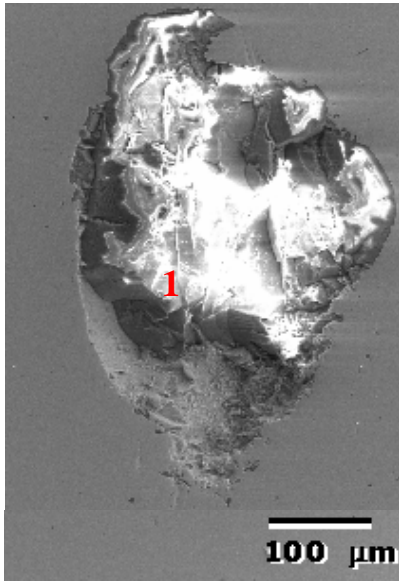


S24



S25

Fig.13 Exogenous inclusions from ladle inner nozzle



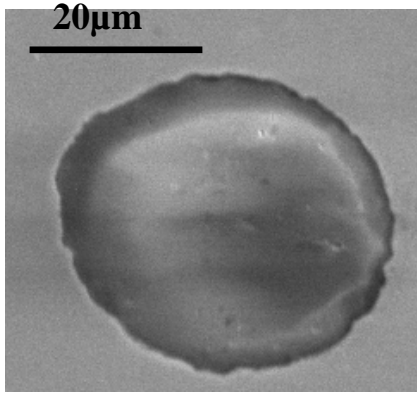
Al₂O₃ 22.05%, SiO₂ 47.02%, MgO 1.88%, CaO 3.15%, FeO 8.51%, MnO 11.95%, K₂O 1.52%, Na₂O 5.07%

1: Al₂O₃ 83.22, MgO 4.36, K₂O 10.26 CaO 2.16
 2: Al₂O₃ 81.05, MgO 3.62, K₂O 10.27, CaO 1.04, FeO 4.03

S26

S27

Fig.14 Inclusions from mold flux and runner brick



S28

Fig.15 Silica based inclusions

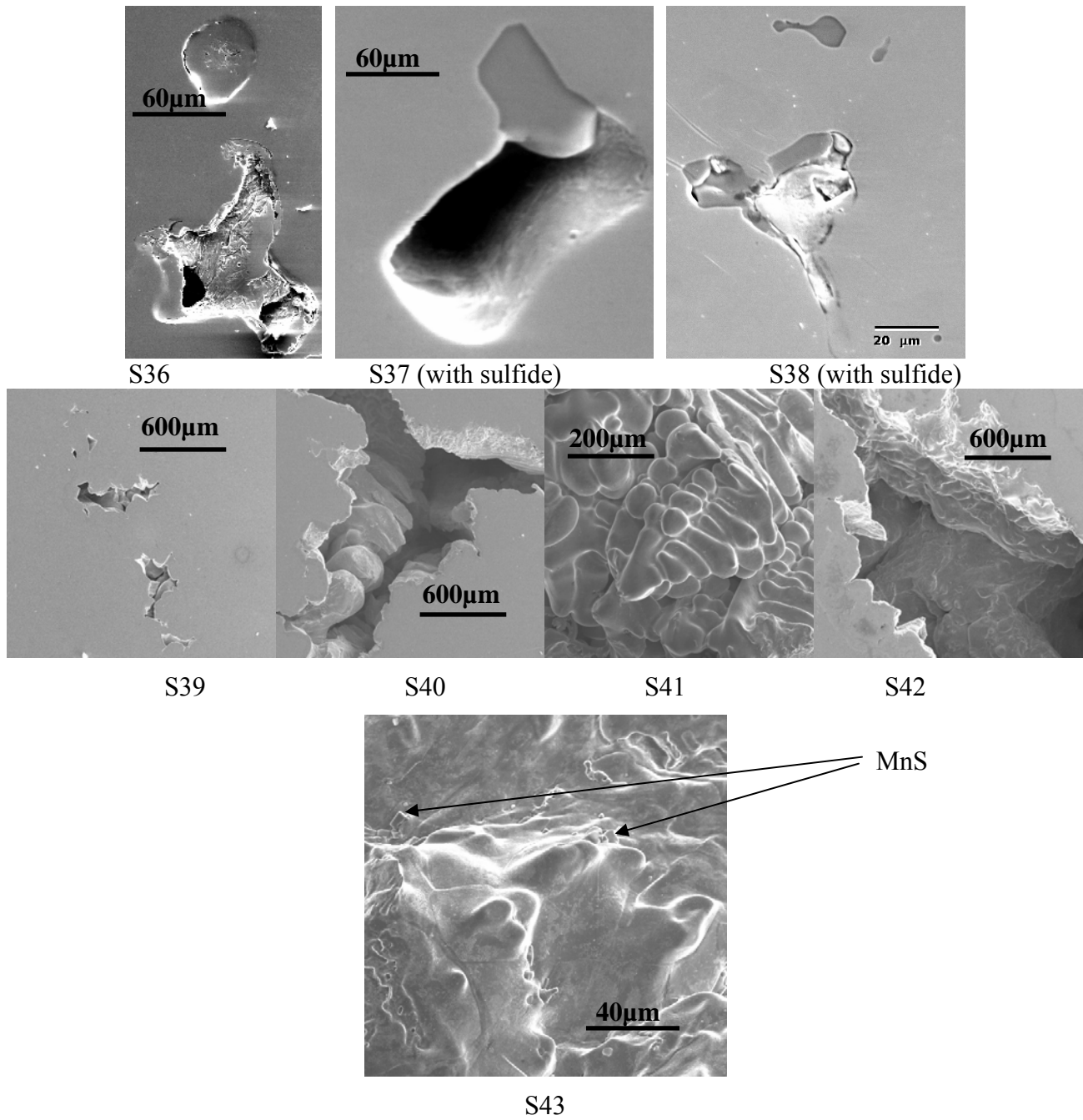
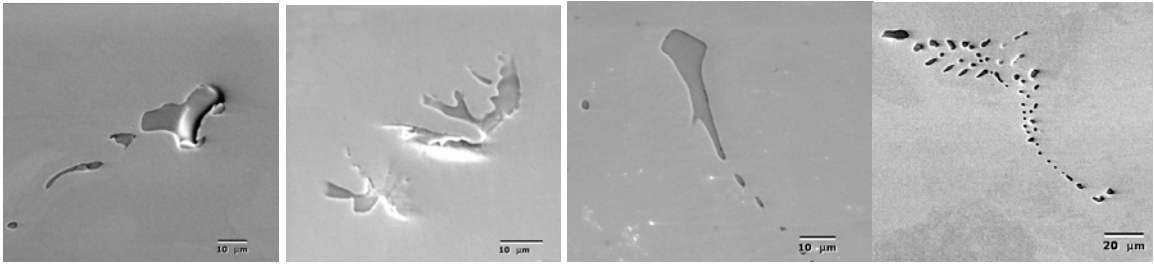


Fig.16 Cavity and holes found on the steel samples

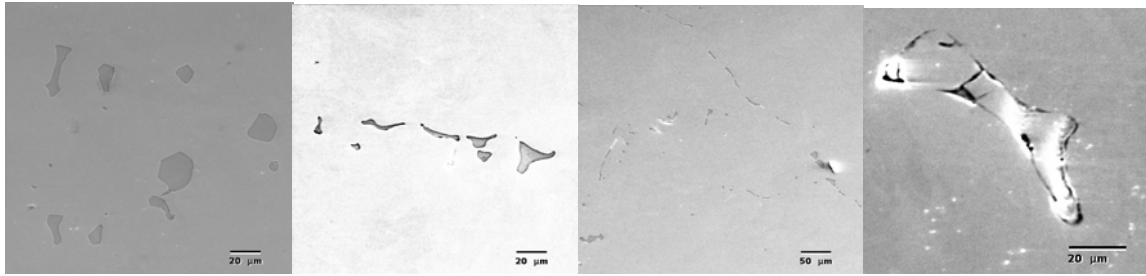


S44

S45

S46

S47



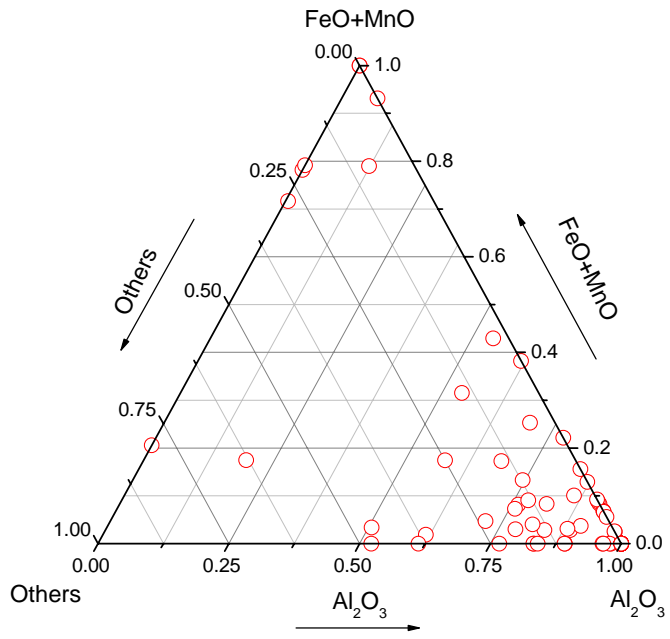
S48

S49

S50

S51

Fig.17 Sulfide inclusions



(Others: MgO+CaO+K₂O+Na₂O+ZrO₂+TiO₂+SiO₂)

Fig.18 Composition of non-sulfide inclusions observed in the samples



Fig.19 Used Runner Brick

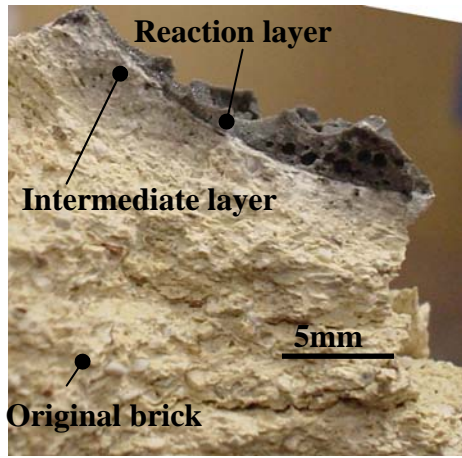


Fig.20 Runner slag

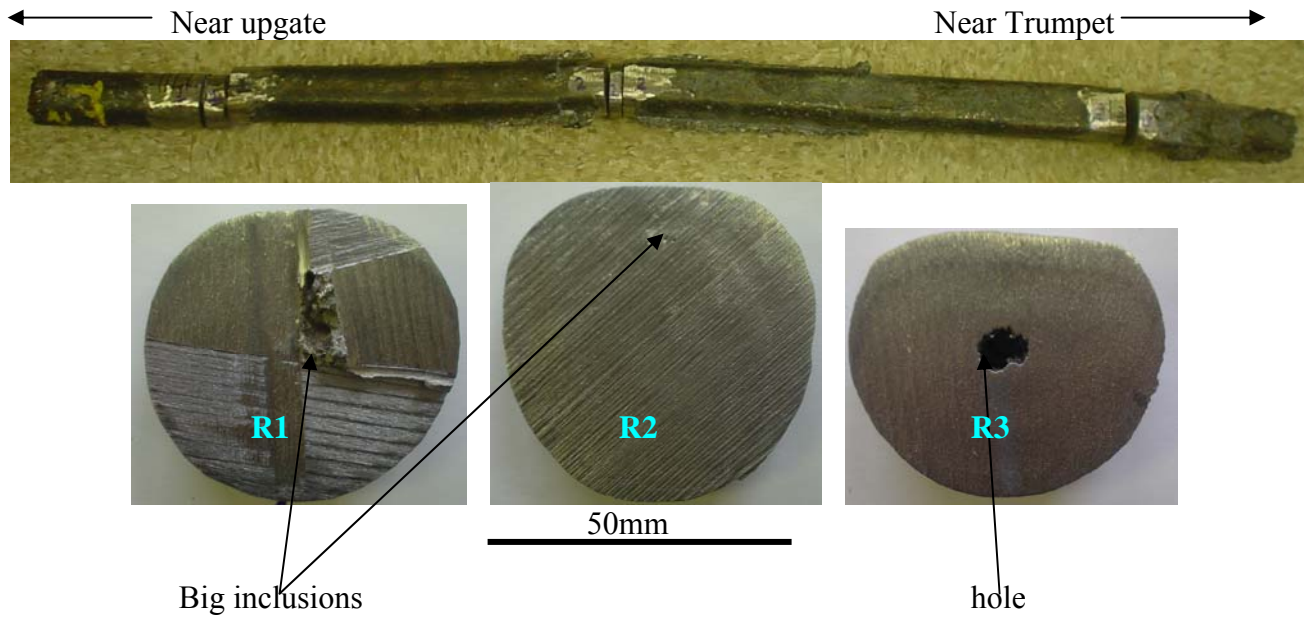
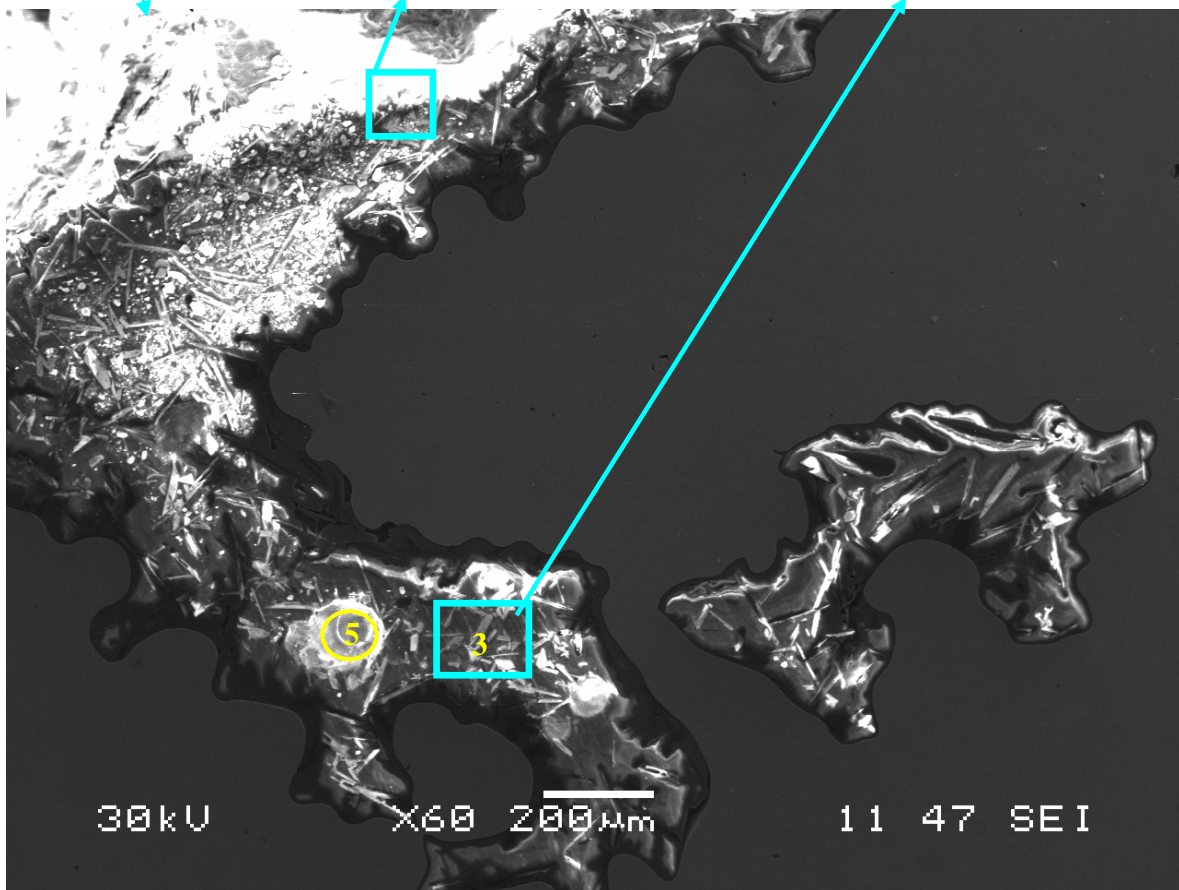
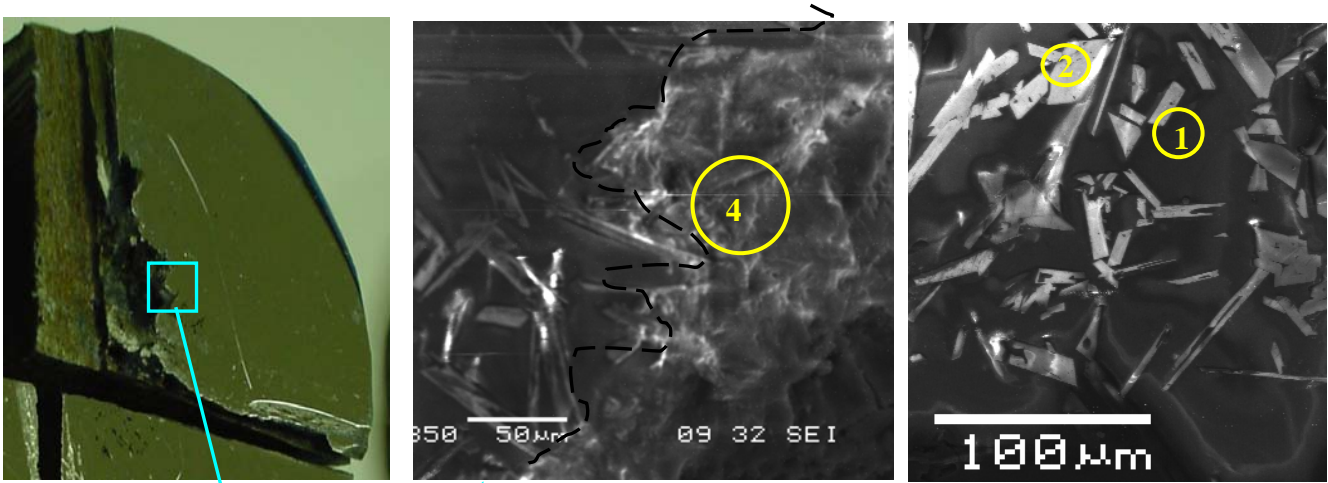


Fig.21 Runner steel samples (near upgate, runner midpoint, and near trumpet from left to right)



	Al ₂ O ₃	SiO ₂	MnO	K ₂ O	Na ₂ O	TiO ₂
1	19.93	40.02	36.23	1.23		2.57
2	100					
3	47.16	32.75	20.09			
4	7.12	78.39	11.21		1.94	
5	3.88	82.4	10.20	1.23	1.39	

Fig.22 MnO-rich inclusions at the center of runner steel samples

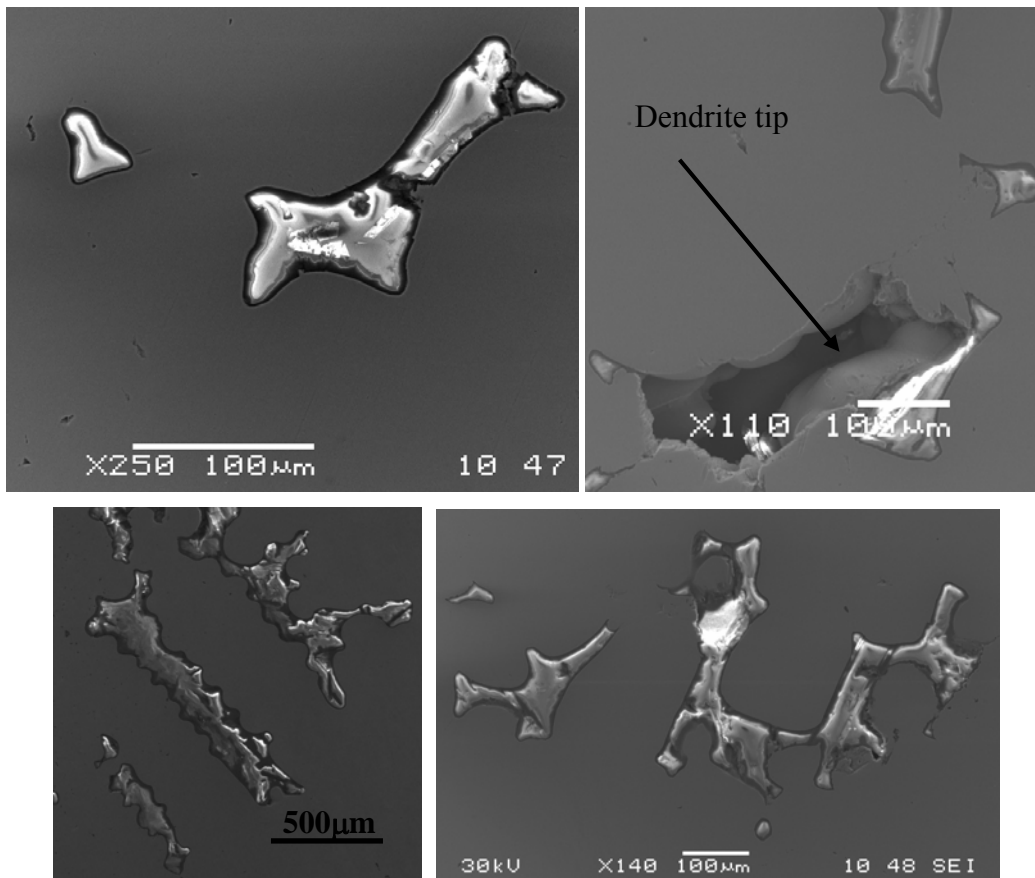


Fig.23 MnO-rich inclusions distribute along the dendritic gap

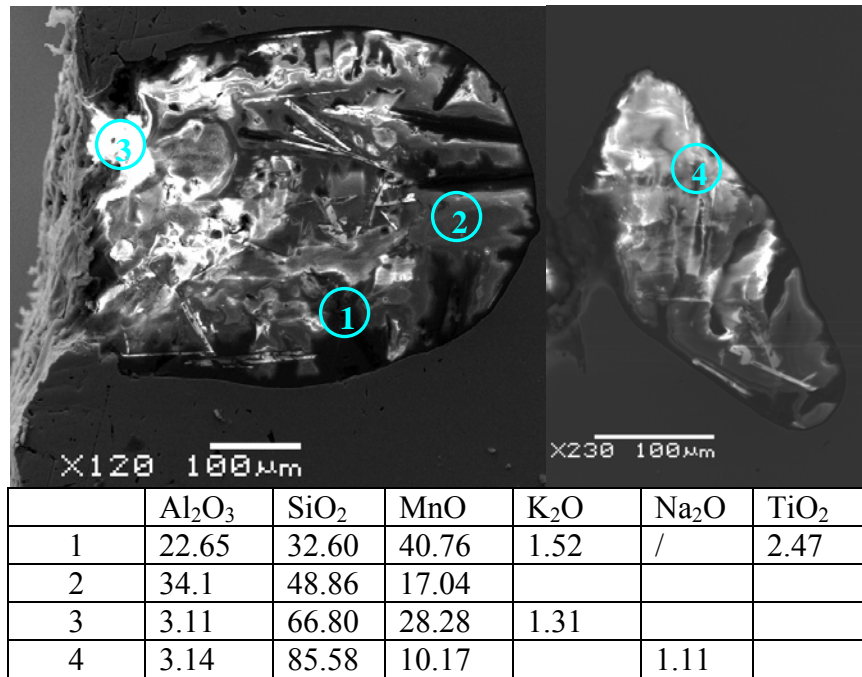


Fig.24 MnO-rich inclusions near the edge of runner steel samples

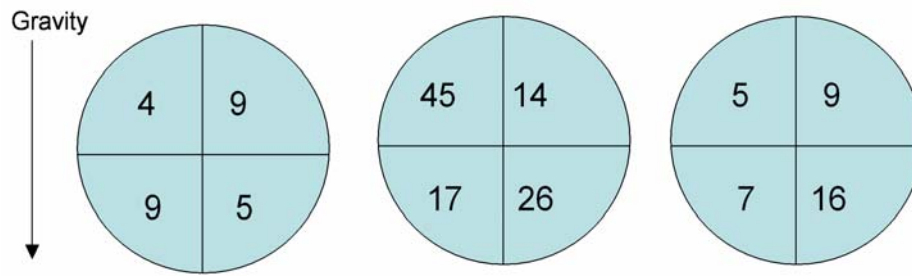


Fig.25 Inclusion distribution on runner steel samples